Radially dependent stray field signature of chiral magnetic skyrmions

Craig Barton,[1,*] Alexander Fernández Scarioni,[2] Baha Sakar,[2] Sibylle Sievers,[2] Felipe Garcia-Sanchez,[3] Phillip Thompson,[4] Fernando Ajejas,[5] William Legrand,[5] Nicolas Reyren,[5] Thomas Thomson,[4] Vincent Cros,[5] Hans W. Schumacher,[2] and Olga Kazakova[1]

[1]*National Physical Laboratory, Teddington TW11 0LW, United Kingdom*

[2]*Physikalisch-Technische Bundesanstalt, 38116 Braunschweig, Germany*

[3]*Departamento Física Aplicada, Universidad de Salamanca, 37008 Salamanca, Spain*

[4]*Nano Engineering and Spintronic Technologies Group, Department of Computer Science, University of Manchester, Oxford Road, Manchester M13 9PL, United Kingdom*

[5]*Unité Mixte de Physique, CNRS, Thales, Université Paris-Saclay, 91767 Palaiseau, France*

(Received 1 February 2022; revised 19 June 2023; accepted 20 June 2023; published 12 September 2023)

Magnetic skyrmions are topological spin structures that arise in chiral magnetic systems which exhibit broken inversion symmetry and high spin-orbit coupling resulting in a sizable Dzyaloshinskii-Moriya interaction. Understanding the local spin texture of skyrmions is a vital metrological step in the development of skyrmionic technologies required for novel logic or storage devices in addition to providing fundamental insight into the nanoscale chiral interactions inherent to these systems. Here, we propose that there exists a radially dependent stray field signature that emanates from magnetic skyrmions. We employ quantitative magnetic force microscopy to experimentally explore this stray field signature. To corroborate the experimental observations a semianalytical model is developed which is validated against micromagnetic simulations. This unique approach provides a route to understand the unique radially dependent field signature from skyrmions, which allows an understanding of the underlying local magnetization profile to be obtained. From a practical standpoint, our results provide a rapid approach to validate outputs from numerical or micromagnetic simulations. This approach could be employed to optimize the complex matrix of magnetic parameters required for fabricating and modeling skyrmionic systems, in turn accelerating the technology readiness level of skyrmionic based devices.

DOI: 10.1103/PhysRevB.108.104409

I. INTRODUCTION

Skyrmions are topologically stable chiral twists of magnetization exhibiting quasiparticlelike properties [1–6]. They have received significant attention from the research community due to their potential use in real-world technological applications and the fundamental insights they can provide into topological phenomena in condensed matter systems [7]. Because skyrmions exhibit a nontrivial topology they are inherently stable leading to several technologically exploitable and desirable attributes [8]. These include the ability to circumvent repulsive pinning potentials created by imperfections in the host thin film [9–11], an energy barrier which prevents the collapse to a field polarized state via a decay path mediated by magnons [12,13], they can be manipulated and moved by current induced spin-orbit torques at low current densities [12–18], and they can be stabilized to sub-10-nm dimensions [19]. These characteristics combined with a decade of intense research activity have established several promising applications [6,20]. Of these, skyrmion based neuromorphic spintronic computing is gaining significant traction with examples of skyrmion synaptic devices [21] and reservoir computing [22,23] recently being reported.

To reliably make use of skyrmions for potential applications, an understanding of the local spin structure and how this can be affected by, for example, local variations of properties within the material [24] is required. Therefore, an understanding of the spin structure is vital in progressing skyrmionic materials and devices into higher levels of technology readiness. There are several measurement techniques available to extract the spin structure of magnetization textures and skyrmions, including spin-polarized scanning tunneling microscopy (SPSTM), Lorentz transmission electron microscopy (LTEM), scanning probe nitrogen vacancy (NV) magnetometry, and x-ray magnetic nanotomography. However, despite their high resolving power, their ability to resolve and determine local skyrmion magnetization or spin texture and extract absolute measurements of the sample stray field [19,25–31] is typically limited to very specific samples, sample preparation, and/or measurement conditions such as synchrotron beamlines [30,32].

An alternate solution is to use a flexible and versatile indirect approach such as magnetic force microscopy (MFM) [33]. In MFM, the signal is due to the force gradient between an oscillating magnetically coated atomic force probe and the stray magnetic field from a sample [32]. The measured

*craig.barton@npl.co.uk

quantity is the resonance phase (frequency) shift between the measured oscillation and mechanical driving force [32,34], which is related to the force gradient by the mechanical properties of the probe [34]. The phase is proportional to the force gradient in the limit of small changes and oscillation amplitudes [32,34]. However, due to the extended nature of the tip, the measured phase contrast is not a direct measure of the local sample magnetic field or magnetization and thus only gives qualitative data. As simple physical models such as point probe models do not, in general, describe the imaging process adequately, a quantitative interpretation of the force interaction to determine the underlying magnetization requires a more complex analysis approach [32,34]. Quantitative magnetic force microscopy (qMFM) allows for a full quantitative description relating the measured force gradient to the tip-sample interaction. Here, we follow the seminal tip transfer function (TTF) approach developed by Hug *et al.* [35] allowing the force exerted by the sample stray field on the MFM tip to be calculated in Fourier space [34–37]. Exploiting a well characterized reference sample, a calibration procedure leads to a model-independent and parameter-free representation of the MFM tip's point spread function (PSF) [32,34]: the TTF. The TTF can be used to determine stray fields from an unknown sample through deconvolution [34] or, as here, the force gradient can be directly calculated using a realistic model of a magnetization texture [37–40]. Recent examples, where qMFM has proven to be an invaluable tool for exploring the properties of magnetic skyrmions, include local determination of the interfacial Dzyaloshinskii-Moriya interaction (DMI) in multilayer $[Ta/Co/Pt]_n$ thin-film systems [40], correlation of skyrmions to their topological Hall effect in $SrIrO_3/SrRuO_3$ bilayers [41], and a multipole expansion approach to distinguish skyrmions in $[Ir/FeCo/Pt]_n$ multilayers [42]. Furthermore, qMFM has recently entered the metrological arena with validated results from round robin measurements reaching consensus across European national metrology institutes (NMIs) [34].

In this work, we present a study reporting on a unique radial dependence of stray magnetic fields emanating from skyrmions. A model is proposed, detailing how the evolution of the stray field spatial frequencies is fundamentally a function of the radius of two-dimensional (2D) magnetic skyrmions. The model is tested by exploring the influence of skyrmion size on the measured MFM response for skyrmions nucleated in a micron-wide stripe comprising of Co/Ru/Pt chiral multilayers. The measured phase shift is correlated to the skyrmion radius revealing a distinct functional dependence. To validate this, qMFM is used to compute the MFM phase shift for an analytical Néel type skyrmion model hosted in a magnetic multilayer thin film, where the radius r and skyrmion domain wall width w are treated as independent variables.

In addition to determining the unique radial dependence of stray magnetic fields emanating from skyrmions, a practical use case is identified which allows us to extract the most probable skyrmion domain wall width (w) and helicity (γ), which describes the local sense of the spin rotation within the domain wall. Our results offer a route to a deeper understanding of the local spin textures, which is of high interest to the skyrmionic community, as reliable and rapid characterization will be required to expedite the fabrication, modeling, and optimization cycle, in turn reducing the timescales to realize real-world devices.

II. QUANTITATIVE MAGNETIC FORCE MICROSCOPY (qMFM)

qMFM relies upon a set of versatile transfer functions that can be used to convert physical quantities such as the sample magnetization to the sample stray field or the force on the tip, via a tip transfer function, in the Fourier domain [34–37]. qMFM requires knowledge of the instrument's transfer function (TF) which is obtained via a calibration procedure. The TF is the product of an instrument calibration factor (ICF) and the TTF, where the ICF introduces the mechanical properties and the physical angle of the cantilever, Θ, with respect to the surface normal [34,36]. The TTF is the Fourier transform of the z component of the magnetic field gradient of the tip, $H_z^{'\,\mathrm{tip}}$; i.e., it relates only to the magnetic properties of the tip [34,35,43] and dictates the spatial resolution and sensitivity of MFM. The TF is denoted as $G(\mathbf{k}, z)$, and is the product of the ICF and TTF, i.e., $\{-\frac{2\,Q\mu_0}{c} \cdot [\mathrm{LCF}\,(k, \Theta)]^2 \cdot \hat{H}_z^{'\,\mathrm{tip}}\,(\mathbf{k}, z)\}$, where $[\mathrm{LCF}\,(\mathbf{k}, \Theta)]^2$ describes the cantilever angle, $\mathbf{k} = (k_x, k_y)$; Q and c are the cantilever oscillation quality factor and stiffness constant, respectively; $\hat{H}_z^{'\,\mathrm{tip}}\,(\mathbf{k}, z)$ is the TTF and μ_0 is the vacuum permeability. The hat is the complex conjugate. In this work, both the ICF and TTF are obtained via measurements of the mechanical properties of the cantilever for the ICF [34–39] and measurements of a well characterized magnetic multilayer reference sample for the TTF [34–39], hence, the total transfer function TF [34,35]. The phase in real space, $\Delta\varphi$, is described by a convolution integral of the tip stray field and the sample magnetization. This is conveniently described by a multiplication in Fourier space, where the coordinates are mapped to a two-dimensional reciprocal space $(x, y, z) \rightarrow (k_x, k_y, z)$, where the z component is retained (partial Fourier space). In Fourier space, $\Delta\varphi$ is given by [34]

$$\begin{aligned}\Delta\Phi(\mathbf{k}, z) &= -\frac{2\,Q}{c} \cdot \mu_0 H_z^{\mathrm{sample}}\,(\mathbf{k}, z) \cdot [\mathrm{LCF}\,(k, \Theta)]^2 \cdot \hat{H}_z^{'\,\mathrm{tip}}\,(\mathbf{k}, z) \\ &= G(\mathbf{k}, z) \cdot H_z^{\mathrm{sample}}(\mathbf{k}, z). \end{aligned} \tag{1}$$

$H_z^{\mathrm{sample}}(\mathbf{k}, z)$ is the sample stray field, which can be computed via a field transfer function from the Fourier components of the magnetization [35]. Therefore, $\Delta\Phi(\mathbf{k}, z)$ is uniquely related to the sample field in the limit of no mutual tip-sample perturbations [32,34]. $H_z^{'\,\mathrm{tip}}\,(\mathbf{k}, z)$ is obtained from a reference measurement of a calibration sample, $\Delta\Phi^{\mathrm{ref}}(\mathbf{k}, z)$, and subsequent deconvolution of $H_z^{\mathrm{sample}}(\mathbf{k}, \mathbf{z})$, from $\Delta\Phi^{\mathrm{ref}}(\mathbf{k}, z)$. As the deconvolution is an ill-posed problem, regularization is introduced in the form of an inverse Wiener filter [32,34,37–40]:

$$\mathrm{TTF}(\mathbf{k}, z) = \frac{\Delta\Phi^{\mathrm{ref}}(\mathbf{k}, z)}{\mathrm{ICF}} \cdot \frac{\hat{H}_z^{\mathrm{sample}}(\mathbf{k}, z)}{\left|H_z^{\mathrm{sample}}(\mathbf{k}, z)\right|^2 + \alpha}. \tag{2}$$

The regularization parameter α reduces the impact of noise on the deconvolution at high spatial frequencies with

low signal to noise ratio. Once $H_z^{'\,\mathrm{tip}}(\mathbf{k}, z)$ is determined, it is possible to deconvolve $H_z^{'\,\mathrm{tip}}(\mathbf{k}, z)$ from a phase shift measurement of a sample under test through further regularized deconvolution to extract the sample stray field distribution [34]. Alternatively, one can compute the spatial distribution of the force acting on the tip by convolving $\hat{H}_z^{'\,\mathrm{tip}}(\mathbf{k}, z)$ with H_z^{sample}, which can be calculated from a model magnetization pattern (through the field transfer function) [37–40] as employed here.

III. SKYRMION STRAY FIELD MODEL AND RADIAL DEPENDENCE

First, we present a simple model for the skyrmion spin texture and the corresponding magnetic stray field that emanates from the magnetic structure. Here, a purely Néel type skyrmion [44] is assumed, where the core magnetization is out of plane and the spins in the skyrmion domain wall rotate away from or towards the core. As such, the in-plane spin components wind chirally, fixing the helicity of the Néel type skyrmion ($\gamma = 0, \pi$), respectively [42], shown schematically in Figs. 1(a) and 1(b). In this work, the spin profile is defined following the work of Romming *et al.* [19], where the angle, θ_{spin}, at position $\rho = \sqrt{x^2 + y^2}$ defines a 360 ° domain wall profile given by $\theta_{\mathrm{spin}}(\rho, r, w) = \sum_{\pm}\{\arcsin[\tanh(\frac{-\rho \pm r}{w})]\} + \pi$. Here, r and w are the effective skyrmion radius and wall width, respectively, and θ_{spin} defines the local magnetization vector by

$$\vec{\boldsymbol{M}}(x, y) = M_s \begin{Bmatrix} -\sin[\theta_{\mathrm{spin}}(\rho, r, w)]x/\rho \\ -\sin[\theta_{\mathrm{spin}}(\rho, r, w)]y/\rho \\ \cos[\theta_{\mathrm{spin}}(\rho, r, w)] \end{Bmatrix}, \tag{3}$$

where M_s is the saturation magnetization. Here, we use $\vec{\boldsymbol{M}}(x, y)$ to define a set of skyrmions where r spans 30–220 nm to match the experimentally observed skyrmions in this work and w spans 1–55 nm to cover a reasonable amount of parameter space in the model.

The mathematical description of the magnetic field is defined by the field transfer function, and fully incorporates the uniform magnetization along the z axis (perpendicular to the sample plane) and the contribution from in-plane magnetization components within the skyrmion domain wall, i.e., $\vec{\boldsymbol{M}}(x, y) = (M_x, M_y, M_z)$. As such, the contributions from magnetic surface charges, $\sigma_{\mathrm{surface}} = \hat{\boldsymbol{n}} \cdot \boldsymbol{M_s}(\mathbf{k})$, and volume charges, $\rho_{\mathrm{Vol}} = -\nabla \cdot \boldsymbol{M}(\mathbf{k})$, are both included in the calculation of the skyrmion stray magnetic field. The z component of the stray magnetic field due to $\sigma_{\mathrm{surface}}$ and ρ_{Vol} in Fourier space is given by [34–37]

$$H_z^{\mathrm{sample}}(\boldsymbol{k}, z) = \frac{e^{-kz}(1 - e^{-kt})}{2}\left(-\frac{\nabla}{k}\right)M(\boldsymbol{k}). \tag{4}$$

Here, $\nabla(\mathbf{k}) = (ik_x, ik_y, -k)$, is the magnetic potential operator in Fourier space [35]. As skyrmions are hosted in a magnetic multilayer in this work (see Supplemental Material [45], and references therein [46–59]), a layered model is constructed to compute $H_z^{\mathrm{sample}}(\boldsymbol{k}, z)$, where the defined skyrmion magnetization is restricted to the magnetic Co layers only. Furthermore, for the thicknesses of the individual magnetic layers considered in this work, ρ_{Vol} is assumed constant throughout the entirety of the magnetic Co layer of thickness t.

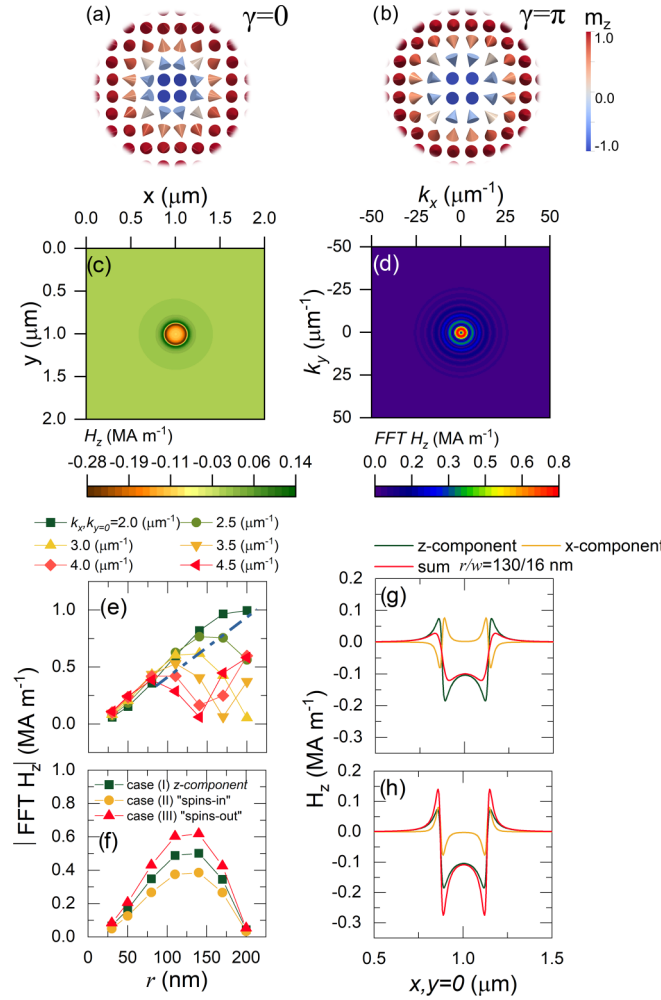

FIG. 1. [(a), (b)] vector fields showing the two distinct skyrmion types considered in this work. (c) Calculated H_z^{sample} for a skyrmion defined by $r = 130$ nm, $w = 16$ nm, and $\gamma = 0$. (d) shows the FFT of the stray magnetic field data in (c). (e) Radial dependence for a selected range of spatial frequency amplitudes (blue dashed line) indicates the trend in the peak data. (f) Radial dependence of the calculated stray field spatial frequency amplitudes for k_x, $k_{y=0} = 3.0$ (μm^{-1}), comparing the radial dependence for cases (I)–(III). [(g), (h)] Line profiles though the separated H_z^{sample} contributions from the z component, in-plane (x), and total sum for all magnetization components (green, yellow, and red lines, respectively). The spin rotation corresponds to cases (II) and (III) ($\gamma = \pi$ and $\gamma = 0$) for [(g), (h)], respectively.

Figure 1(c) introduces the archetypal output from Eq. (4) applied to our layered system demonstrating the stray field for a ($\gamma = 0$) skyrmion with a core pointing in the negative z direction (into the page) defined by our convention to match the experimental case (see Supplemental Material [45]). To expand the model further the spatial frequency content of the stray magnetic field is explored in more detail. Figure 1(d) displays an example fast Fourier transform (FFT) of the data presented in Fig. 1(c) which is used to assess the spatial frequency content for different skyrmion radii and domain

wall widths. To ascertain the role of r and γ on the total stray field, we isolate dominant low spatial frequencies, those with the largest amplitudes in frequency space, that are expected to provide the dominant features of the final stray field profile. Figure 1(e) details the radial dependence of six low spatial frequencies $k_x = 2.0{-}4.5\ \mu\text{m}^{-1}$. These data show a distinct functional form, including in a peak in the stray field over the range of radii (r) calculated. The amplitude of the peak decreases as k_x increases, highlighting the shift in the peak position and the reduced role of higher spatial frequencies in the overall field profile. To explore the effects of ρ_{Vol} and γ, a single spatial frequency ($k_x = 3.0\ \mu\text{m}^{-1}$) was simulated for three cases: (I) surface charge only, σ_{surface}; and two cases including the volume charges ρ_{Vol}, i.e., (II) spin rotation toward the skyrmion core [clockwise (CW) chirality)] ($\gamma = \pi$); and (III) spin rotation away from the skyrmion core [counterclockwise (CCW) chirality] ($\gamma = 0$). The functional form, shown in Fig. 1(e), is further modified, and is found to be dependent on the specific spin texture and their distinct contributions to the spatial frequency components of the stray field. With case (I) as a baseline, it can be seen that cases (II) and (III) either reduce or increase the spatial frequency amplitudes around the peak position, as shown in Fig. 1(f). The perturbation to case (I) results from the nonzero stray field, $\rho_{\text{Vol}} = -\nabla \cdot \boldsymbol{M}(\mathbf{k})$, included in the calculation which is either subtractive from or additive to the field from surface charges (σ_{surface}) alone for (II) or (III), respectively. Figures 1(g) and 1(h) demonstrate this effect in detail where the calculated real-space stray field for cases (II) and (III) are shown in relation to case (I). These data show that the total field is highly dependent on the additional contribution provided by $\rho_{\text{Vol}} = -\nabla \cdot \boldsymbol{M}(\mathbf{k})$ which modifies the stray field originating from σ_{surface}, suppressing or amplifying the stray field due to σ_{surface} for cases (II) or (III), respectively. This results in a stray field signature that is unique and distinguishable and fully dependent on the skyrmion helicity ($\gamma = 0, \pi$).

It is also interesting to note that reducing the skyrmion radius will lead to an increase in the peak stray field above the skyrmion, as expected. However, analysis of the spectral content shows that there is distinct increase in the amplitude of the dominant spatial frequencies in the range $30\ \text{nm} < r < 120\ \text{nm}$. This unique radial dependence in the spatial frequency amplitudes demonstrates a trade-off between the skyrmion aspect ratio (diameter/thickness) and the skyrmion volume which modifies the spatial frequency content of the skyrmion stray field with r. Furthermore, the dependence with r will ultimately limit the smallest skyrmions measurable by MFM, providing a practical implication of this radial response.

As such, it is hypothesized that the radial functional dependence of dominant stray field spatial frequencies could be experimentally realized using MFM. Through quantitative approaches it is further proposed that contributions from ρ_{Vol}, within the skyrmion domain wall, would also be observable by a sufficiently high resolution MFM measurement. Therefore, it is conceivable that qMFM could be employed to ascertain the skyrmion helicity γ and, further, the domain wall width w. To test this, an experiment has been designed to verify the results obtained from the model above.

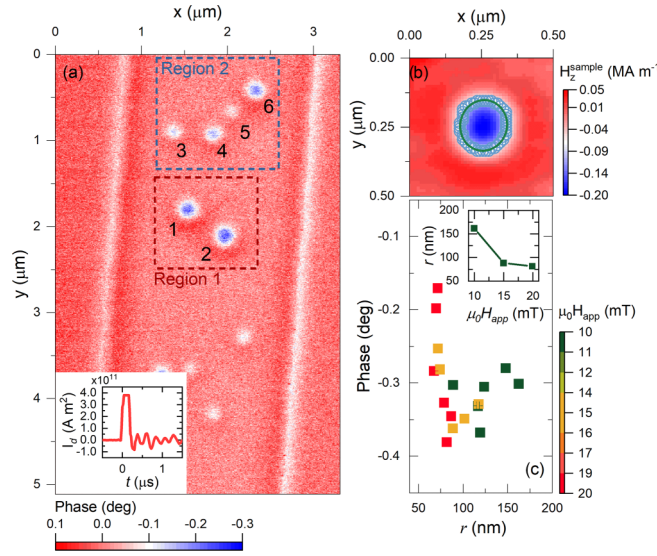

FIG. 2. (a) Magnetic force micrograph detailing the nucleated skyrmions identified for further analysis in this study. Dashed boxes are the scan areas used to minimize the impact of the stripe edge on the measured data. The applied field range to tune the skyrmion size was $\mu_0 H_{\text{app}} = 19.9$, 15.0, and 10.0 mT. Inset shows the applied current pulse used to nucleate skyrmions; where $\mu_0 H_{\text{app}} = 45.5$ mT. (b) H_z^{sample} at the sample surface for skyrmion 2 with $\mu_0 H_{\text{app}} = 19.9$ mT. Superimposed onto the data is the extracted perimeter (blue open circles) and the elliptical implicit fit (green line). (c) Maximum phase response for skyrmions vs r, where the color bar indicates the measurement field for each data point. Inset shows the raw size analysis data with applied field for skyrmion 1.

IV. RADIALLY DEPENDENT PHASE RESPONSE

To establish a set of skyrmions upon which to test our model and hypothesis, we measure a multilayer sample comprising of asymmetric $[\text{Co/Ru/Pt}]_{10}$ trilayers patterned into a 2 μm wide wire (see Supplemental Material [45]). The asymmetric trilayer structure results in a noncanceling Dzyaloshinskii-Moriya interaction (DMI) [60–63] at the interfaces between the magnetic layer and the two heavy metal layers present in our system [64,65]. The DMI and the perpendicular magnetic anisotropy allow the stabilization of skyrmions in perpendicular external magnetic fields. For skyrmion nucleation a combination of an *in situ* perpendicularly applied magnetic field and a rectangular current pulse of width 200 ns [44] is used. Figure 2(a) introduces the skyrmion landscape explored by MFM (see Supplemental Material [45]) and shows an overview of six skyrmions selected to study in this work. Figure 2(a) (inset) shows the current pulse used to nucleate the skyrmions. Tuning the skyrmion size was achieved by varying the *in situ* applied magnetic field throughout the measurement sequence. Three out of plane applied fields, of decreasing magnitude, were chosen resulting in a range of skyrmion sizes. At each field, the regions were scanned ten times to minimize local metastability and to fully relax the skyrmions such that local pinning and tip-sample interactions would not affect further quantitative analysis.

Possible radially dependent phenomena are identified by correlating the maximum phase response from all skyrmions as a function of r at each applied measurement field. The field dependent skyrmion size was extracted using the skyrmion stray field distribution H_z^{sample}, which is obtained through a regularized deconvolution of the measured force gradient data with the TTF, Eq. (2) (see Supplemental Material [45]). Image processing was employed to extract the perimeter of the skyrmion using a Laplacian edge detection filter to define a contour from H_z^{sample}. Figure 2(b) shows example data from the edge detection, where H_z^{sample} is overlaid with the extracted edge data and implicit fit to the elliptical profile. The semimajor and semiminor axes of the implicit elliptical fits were averaged resulting in r (the effective skyrmion radius). The peak phase response was approximated by a single or double Gaussian function using nonlinear least square fitting to find the overall maximum value. The data were numerically ordered with respect to the effective radius r, Fig. 2(c). A clear relationship between the maximum phase response and r is observed, where a maximum interaction (minimum in the data) occurs at an effective radius of ≈120 nm. A strong resemblance to the proposed radial dependence data (Sec. III), is observed and is explored in more detail (Sec. V). The color mapped data detail the progression of the skyrmion size as a function of decreasing applied field magnitude for the two regions of interest, Fig. 2(a). At these length scales, the skyrmion radius r is mostly determined by the competition between Zeeman energy due to $\mu_0 H_{\text{app}}$, which contracts r, and the magnetostatic energy due to internal dipolar interactions, which tends to increase r or even cause it to "blow up" to a stripe domain phase [12]. Therefore, a reduced Zeeman energy, decreasing $\mu_0 H_{\text{app}}$, leads to an increase in r, inset of Fig. 2(c). However, due to the local pinning landscape which varies for each skyrmion [21,24,40], there are varying degrees to the expansion. This is evident in the variance in the data presented in Fig. 2(c), where some smaller skyrmions occur at lower applied fields, indicating that skyrmion expansion is hindered by local pinning.

Analysis of the peak phase signal for a range of skyrmion sizes yields a distinct set of data with a functional form that is comparable to that presented in the spatial frequency analysis from our model. To expound on the experimentally observed radially dependent signature, the proposed model has been extended to calculate the expected MFM signal and comparisons made to the experimental data (below).

V. CALCULATED PHASE RESPONSE: ROLE OF r AND w

To assess the validity of the assumptions (Sec. III) and expound on the functional form of the experimentally observed peak, Fig. 2, the expected MFM phase shift is explored for a range of values of r, w, and γ. To achieve this, we convolve the calculated skyrmion stray field $H_z^{\text{sample}}(\boldsymbol{k}, z)$ [Eq. (4)] with the experimentally determined TF (see Supplemental Material [45]) such that the underlying magnetization (spin texture) is mapped to the theoretical experimental phase. Figure 3(a) details example data of the maximum calculated phase response for case (III). It is observed that the maximum phase response exhibits a peak in the tip-sample interaction (minima in the data) with r. The functional form of these data closely follows that of the experimentally determined radially dependent data, Fig. 2(c), and is indicative of the underlying radial response exhibited by dominant spatial frequencies demonstrated by our stray field calculations, Fig. 1. Interestingly, w is also found to play an important role in the expected phase response and modifies the amplitude and width of the observed peak values. Therefore, the amplitude and width of the experimentally observed radially dependent peak phase data will contain information on the underlying domain wall width.

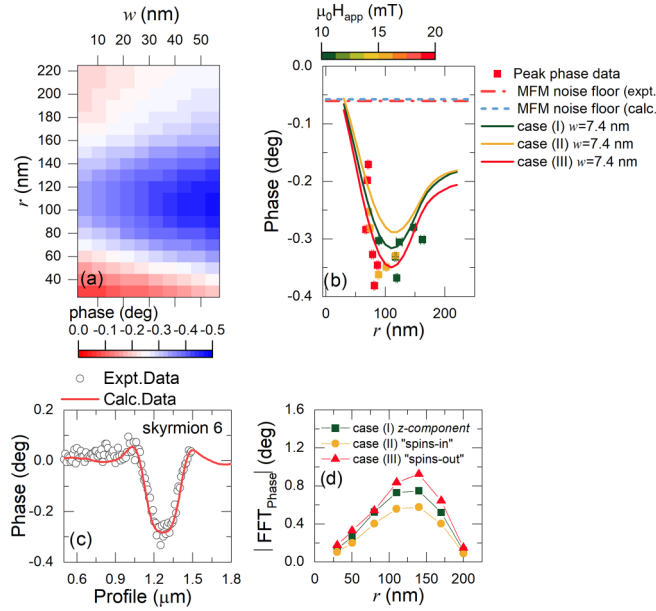

FIG. 3. (a) Maximum calculated phase vs r and w, case (III). (b) Comparison of the calculated maximum skyrmion phase for cases (I), (II), and (III), respectively. The experimental data (squares) are replotted with the calculated phase vs r for the best-fit value of $w = 7.4$ nm. Red and blue dashed lines show the experimental and calculated noise floor. (c) Comparison of skyrmion line profile for experimental (black circles) and calculated (red line) data, for skyrmion 6, where $w = 7.4$ nm [case (III)]. (d) Radial dependence of the calculated phase spatial frequency amplitudes for k_x, $k_{y=0} = 3.0$ (μm^{-1}), comparing the radial dependence for cases (I)–(III).

To test this, the experimentally determined radial response, Fig. 2(c), is compared against the calculated phase response for cases (I)–(III) where the role of w, hence ρ_{Vol}, is explored, Fig. 3(b). Here, we use the residual sum of squares with w as the fitting parameter to find the best-fit case to the data (see Supplemental Material [45]). For the measurement setup and sample combination used in this work, case (III) and $w = 7.4$ nm yields the best fit to the data, red line Fig. 3(b). This agrees with the expected sign of the DMI physically imposed by the stacking order in the asymmetric [Co/Ru/Pt] trilayer, which dictates that for the skyrmion core pointing in the $-z$ direction, a helicity of $\gamma = 0$ will arise.

Along with the best-fit case we also plot the corresponding calculated curves for cases (I) and (II), yellow and green lines, respectively. We find that accounting for the stray field from case (I) only is overly simplistic to capture the full magnitude of the maximum experimental phase. This is reflected in the

residual sum of squares data which has a flat response with w (see Supplemental Material [45]). However, this simplified model does capture the radial dependence which reflects the evolution of the spatial frequencies from the skyrmion that contribute to the convolution with the TF. Considering case (II), we observe a suppression in the phase response from the spins within the domain wall. Additionally, the residual sum of squares quickly diverges with respect to case (III) due to the helicity considered for case (II) and provides strong evidence that case (III) ($\gamma = 0$) best represents the physical system studied in this work. As highlighted previously, it is apparent that for cases (II) or (III), the maximum phase response is suppressed or amplified, respectively, when compared to case (I). This results from the nonzero stray field, $\rho_{\mathrm{Vol}} = -\nabla \cdot \boldsymbol{M}(\mathbf{k})$, which is either subtractive from or additive to the field from $\sigma_{\mathrm{surface}}$ for (II) or (III), respectively [35].

Figure 3(c) shows example phase data for $r_{\mathrm{calc}} = 150$ nm and $r_{\mathrm{expt}} = 147.6$ nm, respectively, for the best-fit case $w = 7.4$ nm. Here, excellent agreement is obtained between the experimental and calculated phase data and provides additional evidence to support the skyrmion model developed in this work.

To assess how the measurement process could affect the radially dependent signature, the spatial frequency amplitudes ($k_x = 3.0\ \mu\mathrm{m}^{-1}$) for the calculated phase are plotted for cases (I)–(III), Fig. 3(d). It is found that the functional form is close to identical to that shown for the spatial frequency amplitudes for the calculated stray field, Fig. 1(f). This corroborates the proposal that the underlying skyrmion magnetization leads to a radially dependent stray field signature. It further confirms that the measured trend is due to the skyrmion stray field and precludes any potential field induced modification due to the measurement process (see Supplemental Material [45].

It is also possible to extract the minimum detectable skyrmion, for our measurement setup and sample combination, using the data in Fig. 3(b). It is found that $r_{\mathrm{min}} \approx 27$ nm, for $w = 7.4$ nm, and agrees well with our noise analysis for the MFM measurement and setup (see Supplemental Material [45]). As such, our data demonstrate the applicability of qMFM as a technique to study highly technologically relevant sub-30-nm skyrmions in ambient measurement conditions, subject to energy stability considerations [44].

To draw conclusions regarding the results from Fig. 3, the skyrmion model is extended to calculate the expected experimental phase employing qMFM techniques. Following this approach, the underlying magnetization texture of the skyrmion is revealed with remarkable detail, allowing the skyrmion helicity (γ) and the domain wall width (w) to be extracted. The results indicate that the evolution of the underlying spatial frequency content of the skyrmion stray field with r modifies the tip-sample interaction and not potential field induced changes to the MFM tip.

VI. MICROMAGNETIC SIMULATIONS

To explore the validity of the simple model and calculated MFM phase response, micromagnetic simulations

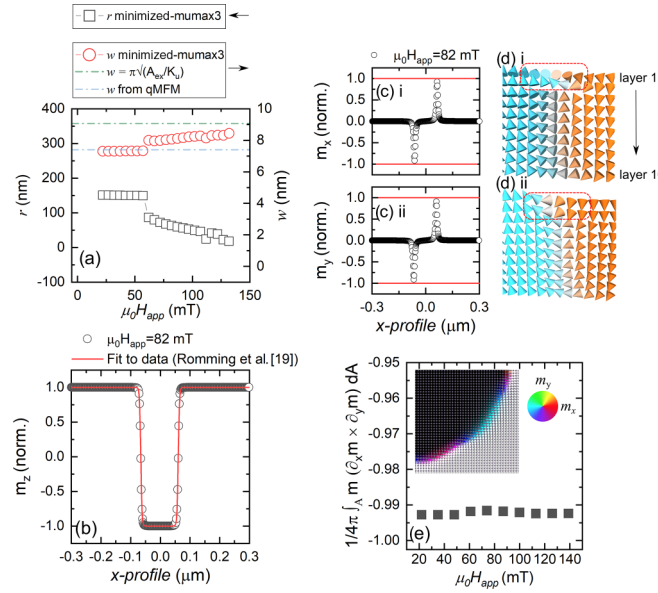

FIG. 4. (a) Micromagnetic results showing r, left axis (black squares), and w, right axis (red circles), as a function of applied magnetic field. (b) shows example profile data (black circles) for the m_z component of magnetization at $\mu_0 H_{\mathrm{app}} = 82$ mT. Red line is a fit to the data using Eq. (3). (c) i and ii show stack averaged line profiles for the m_x, m_y components of magnetization, respectively. (d) i and ii show x, y slices through the spin vector field, respectively, showing the domain wall transition (color scale indicates m_z). (e) shows the stack averaged Q with H_{app} and the inset is the spin vector field for a ≈0.25 section of the skyrmion in layer 1.

have been performed using the open-source micromagnetic framework MUMAX3 (see Supplemental Material [45], and [66]). Figure 4(a) shows extracted r and w values from a set of simulations, black squares and red circles, respectively. To tune the range of skyrmion sizes, an applied field was used to match the range of r from the experimentally measured data. The dashed lines show domain wall widths for the expected magnetic parameters considered and the value obtained from the qMFM experiments, Fig. 3(b). Over the radii considered in our micromagnetic simulations, 18−150 nm, w remains constant, $w \approx 7.9 \pm 0.5$ nm. This value is in excellent agreement with the extracted best-fit case, $w = 7.4$ nm, and corroborates our simple model approximation where r and w are treated independently and w is fixed over the full range of r. As such it is evidenced that the simple model approximation is valid within the experimental range considered here. Furthermore, quantitative LTEM measurements on very similar films yield values of $w = 5 \pm 1$ nm [67], which is highly comparable to the measurements made here using qMFM. Figure 4(b) shows the averaged z component of the magnetization and expounds on the approach to extract r and w using Eq. (3).

Our simulations reveal that when fixing the skyrmion core in the $-z$ direction, the rotation of the spins in the domain wall point outward for the magnetic parameters used in the simulation. This agrees with the conclusion reached from the best-fit case, Fig. 3(b) where the stacking order of the layers

used in this work, and hence the sign of the DMI, lead to a skyrmion described by case (III) ($\gamma = 0$). Figures 4(ci) and 4(cii) show profiles of the averaged x and y components of magnetization revealing a predominantly Néel type skyrmion which is in good agreement with the skyrmion ansatz assumed in this work.

Closer examination of the local magnetic moments in the wall shows that the Néel type behavior deviates from this trend close to the sample surface (layers 1 and 2). This is shown by the corresponding x, y slices of the spin vectors, Figs. 4(di) and 4(dii), respectively. Twists away from the Néel type character are evidenced as detailed in the top two surface layers. This agrees with the work presented by Legrand *et al.* [27,44], where it is demonstrated that competition between interlayer magnetostatic and interfacial Dzyaloshinskii-Moriya interactions (iDMI) leads to hybrid chiral walls for iDMI values below a threshold value, $\approx 2.5\,\mathrm{mJ\,m^{-2}}$ for a comparable multilayer system, as used here [27]. To quantify the deviation from the ideal model the layer dependent topological charge $Q = \frac{1}{4\pi}\int_A \boldsymbol{m}\cdot(\partial_x\boldsymbol{m}\times\partial_y\boldsymbol{m})dA$ with applied magnetic field is plotted, Fig. 4(e). Here, the average field dependent Q is found to be constant and is approximately -1 within numerical errors. We do find a reduction in Q in the layers at the sample surface commensurate with the cross-sectional views, Fig. 4(d). This is more pronounced for the last layer, for intermediate fields, and further highlights the reduced integrity of the uniform domain wall transition that appears in the topmost layers. This is shown in more detail by the spin vector field for layer 1, Fig. 4(e), inset, where only one quadrant is shown. For the parameters simulated, evidence of Bloch lines [68] in this topmost layer are found. However, these do not significantly impact the stack averaged Q.

The results from the micromagnetic simulations validate that the simple, purely Néel type, spin texture that is uniform throughout the layered stack is an accurate approximation to model skyrmions in the $[\mathrm{Co/Ru/Pt}]_{10}$ multilayer system used in this work.

VII. SUMMARY

A simple model for the stray field from a skyrmion hosted in a magnetic multilayer thin film is proposed. By exploring the parameter space of the model, we have found a unique radial functional dependence of the amplitudes of dominant stray field spatial frequencies. We have shown that this response could be experimentally observed by MFM. Furthermore, we have also shown that it has practical implications for skyrmion metrology, such that it is possible to extract the skyrmion helicity and domain wall width with relative ease. To do this a set of experiments employing qMFM has been used to investigate the radially dependent phase response from a set of skyrmions in a chiral magnetic multilayer comprising of $[\mathrm{Co/Ru/Pt}]_{10}$ trilayers. Following this approach, we find that a distinct and unique relationship between the skyrmion radius r and maximum MFM phase response exists. This unique response is due to the evolution of the underlying spatial frequency content of the skyrmion stray field as a function of its radius, which, as we have demonstrated here, modifies and dominates the tip-sample interaction.

We extend our analysis to explore the role of r and w in the calculated expected phase shift and compare the model results with the experimental data. Following this approach, we find a practical implication of the fundamental understanding of the radial dependence and show that we can distinguish the skyrmion type, which for our system is a Néel type with CCW chirality ($\gamma = 0$). Additionally, this methodology provides a unique way to extract the domain wall width of the skyrmions in a multilayer based system. By utilizing a residual sum of squares approach, we find a domain wall width of $w \approx 7.4$ nm. As such, this method provides a simple experimental analog to determine parameters, such as w, in comparison to other approaches such as numerical modeling [40,42,69].

Our results show how the unique evolution of unique stray field signatures from novel nanoscale magnetic solitons can be utilized to interrogate the underlying magnetization structure of technologically relevant skyrmion systems. As shown here, this can be achieved experimentally such that the results could be exploited to validate or inform results from numerical or micromagnetic simulations and other experimental techniques.

We anticipate that this work will provide a high throughput methodology to help to expedite the process to optimize the magnetic parameters used for modeling and fabricating skyrmionic systems, in turn expediting skyrmion based technological development to higher readiness levels.

ACKNOWLEDGMENTS

This project, Project No. 17FUN08 TOPS, has received funding from the EMPIR program cofinanced by the Participating States and from the European Union's Horizon 2020 research and innovation program. The project also received financial support from the UK government department for Business, Energy and Industrial Strategy through NMS funding (Low Loss Electronics) and the UK national Quantum Technologies program. The work was cofunded by the Deutsche Forschungsgemeinschaft under Germany's Excellence Strategy—EXC-2123, QuantumFrontiers—390837967, and the DFG Priority Program No. SPP 2137 Skyrmionics. Financial support from the Agence Nationale de la Recherche, France, under Grant Agreements No. ANR-17-CE24-0025 (TOPSKY) and No. ANR-20-CE42-0012 (MEDYNA), and FET-Proactive Grant Agreement No. 824123 (SKYTOP) is acknowledged. C.B. is indebted to Dr. Volker Neu for use of the stripe domain magnetic reference sample ($[\mathrm{Co/Pt}]_{100}$ d4015). C.B. is further grateful to Dr. Agustina Asenjo for her donation of the GPNT nanorod MFM probes used in this study.

The authors declare no conflict of interest.

[1] A. Bogdanov and D. A. Yablonskii, Thermodynamically stable vortices in magnetically ordered crystals. The mixed state of magnets, Zh. Eksp. Teor. Fiz. **95**, 178 (1989) [Sov. Phys. JETP **68**, 101 (1989)], http://www.jetp.ras.ru/cgi-bin/dn/e_068_01_0101.pdf.

[2] A. Bogdanov and A. Hubert, Thermodynamically stable magnetic vortex states in magnetic crystals, J. Magn. Magn. Mater. **138**, 255 (1994).

[3] U. K. Rößler, A. N. Bogdanov, and C. Pfleiderer, Spontaneous skyrmion ground states in magnetic metals, Nature (London) **442**, 797 (2006).

[4] A. Fert, N. Reyren, and V. Cros, Advances in the physics of magnetic skyrmions and perspective for technology, Nat. Rev. **2**, 17031 (2017).

[5] K. Everschor-Sitte, J. Masell, R. M. Reeve, and M. Kläui, Perspective: Magnetic skyrmions—overview of recent progress in an active research field, J. Appl. Phys. **124**, 240901 (2018).

[6] X. Zhang, Y. Zhou, K. M. Song, T.-E. Park, J. Xia, M. Ezawa, X. Liu, W. Zhao, G. Zhao, and S. Woo, Skyrmion-electronics: Writing, deleting, reading and processing magnetic skyrmions toward spintronic applications, J. Phys.: Condens. Matter. **32**, 143001 (2020).

[7] W. Jiang, G. Chen, K. Liu, J. Zang, S. G. E. te Velthuis, and A. Hoffmann, Skyrmions in magnetic multilayers, Phys. Rep. **704**, 1 (2017).

[8] S.-G. Je, H.-S. Han, S. K. Kim, S. A. Montoya, W. Chao, I.-S. Hong, E. E. Fullerton, K.-S. Lee, K.-J. Lee, M.-Y. Im, and J.-I. Hong, Direct demonstration of topological stability of magnetic skyrmions via topology manipulation, ACS Nano **14**, 3251 (2020).

[9] S. Lin, C. Reichhardt, C. D. Batista, and A. Saxena, Particle model for skyrmions in metallic chiral magnets: Dynamics, pinning, and creep, Phys. Rev. B. **87**, 214419 (2013).

[10] A. Rosch, Skyrmions: Moving with the current, Nat. Nanotechnol. **8**, 160 (2013).

[11] J. Sampaio, V. Cros, S. Rohart, A. Thiaville, and A. Fert, Nucleation, stability and current-induced motion of isolated magnetic skyrmions in nanostructures, Nat. Nanotechnol. **8**, 839 (2013).

[12] F. Büttner, I. Lemesh, and G. S. D. Beach, Theory of isolated magnetic skyrmions: From fundamentals to room temperature applications, Sci. Rep. **8**, 4464 (2018).

[13] A. O. Leonov and M. Mostovoy, Edge states and skyrmion dynamics in nanostripes of frustrated magnets, Nat. Commun. **8**, 14394 (2017).

[14] W. Jiang, X. Zhang, G. Yu, W. Zhang, X. Wang, M. B. Jungfleisch, J. E. Pearson, X. Cheng, O. Heinonen, K. L. Wang, Y. Zhou, A. Hoffmann, and S. G. E. te Velthuis, Direct observation of the skyrmion Hall effect, Nat. Phys. **13**, 162 (2017).

[15] W. Legrand, D. Maccariello, N. Reyren, K. Garcia, C. Moutafis, C. Moreau-Luchaire, S. Collin, K. Bouze-houane, V. Cros, and A. Fert, Room-temperature current-induced generation and motion of sub-100 nm skyrmions, Nano Lett. **17**, 2703 (2017).

[16] R. Juge, S.-G. Je, D. de Souza Chaves, L. D. Buda-Prejbeanu, J. Peña-Garcia, J. Nath, I. M. Miron, K. G. Rana, L. Aballe, M. Foerster, F. Genuzio, T. O. Mentes, A. Locatelli, F. Maccherozzi, S. S. Dhesi, M. Belmegue-nai, Y. Roussigné, S. Auffret, S. Pizzini, G. Gaudin *et al.*, Current Driven Dynamics of Magnetic Skyrmions in an Ultrathin Film, Phys. Rev. Appl. **12**, 044007 (2019).

[17] K. Zeissler, S. Finizio, C. Barton, A. J. Huxtable, J. Massey, J. Raabe, A. V. Sadovnikov, S. A. Nikitov, R. Brearton, T. Hesjedal, G. van der Laan, M. C. Rosamond, E. H. Linfield, G. Burnell, and C. H. Marrows, Diameter-independent skyrmion Hall angle observed in chiral magnetic multilayers, Nat. Commun. **11**, 428 (2020).

[18] K. Litzius, J. Leliaert, P. Bassirian, D. Rodrigues, S. Kromin, I. Lemesh, J. Zazvorka, K.-J. Lee, J. Mulkers, N. Kerber, D. Heinze, N. Keil, R. M. Reeve, M. Weigand, B. V. Waeyenberge, G. Schütz, K. Everschor-Sitte, G. S. D. Beach, and M. Kläui, The role of temperature and drive current in skyrmion dynamics, Nat. Electron. **3**, 30 (2020).

[19] N. Romming, A. Kubetzka, C. Hanneken, K. V. Bergmann, and R. Wiesendanger, Field-Dependent Size and Shape of Single Magnetic Skyrmions, Phys. Rev. Lett. **114**, 177203 (2015).

[20] C. Back, V. Cros, H. Ebert, K. Everschor-Sitte, A. Fert, M. Garst, T. Ma, S. Mankovsky, T. L. Monchesky, M. Mostovoy, N. Nagaosa, S. S. P. Parkin, C. Pfleiderer, N. Reyren, A. Rosch, Y. Taguchi, Y. Tokura, K. von Bergmann, and J. Zang, The 2020 skyrmionics roadmap, J. Phys. D: Appl. Phys. **53**, 363001 (2020).

[21] K. M. Song, J.-S. Jeong, B. Pan, X. Zhang, J. Xia, S. Cha, T.-E. Park, K. Kim, S. Finizio, J. Raabe, J. Chang, Y. Zhou, W. Zhao, W. Kang, H. Ju, and S. Woo, Skyrmion-based artificial synapses for neuromorphic computing, Nat. Electron. **3**, 148 (2020).

[22] D. Pinna, F. Abreu Araujo, J.-V. Kim, V. Cros, D. Querlioz, P. Bessiere, J. Droulez, and J. Grollier, Skyrmion Gas Manipulation for Probabilistic Computing, Phys. Rev. Appl. **9**, 064018 (2018).

[23] D. Pinna, G. Bourianoff, and K. Everschor-Sitte, Reservoir Computing with Random Skyrmion Textures, Phys. Rev. Appl. **14**, 054020 (2020).

[24] C. Reichhardt and C. J. O. Reichhardt, Plastic flow and the skyrmion Hall effect, Nat. Commun. **11**, 738 (2020).

[25] S. McVitie, S. Hughes, K. Fallon, S. McFadzean, D. McGrouther, M. Krajnak, W. Legrand, D. Maccariello, S. Collin, K. Garcia, N. Reyren, V. Cros, A. Fert, K. Zeissler, and C. H. Marrows, A transmission electron microscope study of Néel skyrmion magnetic textures in multilayer thin film systems with large interfacial chiral interaction, Sci. Rep. **8**, 5703 (2018).

[26] Y. Dovzhenko, F. Casola, S. Schlotter, T. X. Zhou, F. Büttner, R. L. Walsworth, G. S. D. Beach, and A. Yacoby, Magnetostatic twists in room-temperature skyrmions explored by nitrogen-vacancy center spin texture reconstruction, Nat. Commun. **9**, 2712 (2018).

[27] W. Legrand, J.-Y. Chauleau, D. Maccariello, N. Reyren, S. Collin, K. Bouzehouane, N. Jaouen, V. Cros, and A. Fert, Hybrid chiral domain walls and skyrmions in magnetic multilayers, Sci. Adv. **4**, 1 (2018).

[28] I. Gross, W. Akhtar, A. Hrabec, J. Sampaio, L. J. Martínez, S. Chouaieb, B. J. Shields, P. Maletinsky, A. Thiaville, S. Rohart, and V. Jacques, Skyrmion morphology in ultrathin magnetic films, Phys. Rev. Mater. **2**, 024406 (2018).

[29] A. Finco, A. Haykal, R. Tanos, F. Fabre, S. Chouaieb, W. Akhtar, I. Robert-Philip, W. Legrand, F. Ajejas, K. Bouzehouane, N. Reyren, T. Devolder, J.-P. Adam, J.-V. Kim, V. Cros, and V. Jacques, Imaging non-collinear antiferromagnetic textures via single spin relaxometry, Nat. Commun. **12**, 767 (2021).

[30] C. Donnelly, S. Gliga, V. Scagnoli, M. Holler, J. Raabe, L. J. Heyderman, and M. Guizar-Sicairos, Tomographic reconstruction of a three-dimensional magnetization vector field, New J. Phys. **20**, 083009 (2018).

[31] C. Donnelly, S. Finizio, S. Gliga, M. Holler, A. Hrabec, M. Odstrčil, S. Mayr, V. Scagnoli, L. J. Heyderman, M. Guizar-Sicairos, and J. Raabe, Time-resolved imaging of three-dimensional nanoscale magnetization dynamics, Nat. Nanotechnol. **15**, 356 (2020).

[32] O. Kazakova, R. Puttock, C. Barton, H. Corte-León, M. Jaafar, V. Neu, and A. Asenjo, Frontiers of magnetic force microscopy, J. Appl. Phys. **125**, 060901 (2019).

[33] Y. Martin and H. K. Wickramasinghe, Magnetic imaging by "force microscopy" with 1000 Å resolution, Appl. Phys. Lett. **50**, 1455 (1987).

[34] X. Hu, G. Dai, S. Sievers, A. Fernández-Scarioni, H. Corte-León, R. Puttock, C. Barton, O. Kazakova, M. Ulvrc P. Klapetek, M. Havlíček, D. Nečas, Y. Tang, V. Neu, and H. W. Schumacher, Round robin comparison on quantitative nanometer scale magnetic field measurements by magnetic force microscopy, J. Magn. Magn. Mater. **511**, 166947 (2020).

[35] H. J. Hug, B. Stiefel, P. J. A. van Schendel, A. Moser, R. Hofer, S. Martin, and H.-J. Güntherodt, S. Porthun, L. Abelmann, J. C. Lodder, G. Bochi, and R. C. O'Handley, Quantitative magnetic force microscopy on perpendicularly magnetized samples, J. Appl. Phys. **83**, 5609 (1998).

[36] P. J. A. van Schendel, H. J. Hug, B. Stiefel, S. Martin, and H.-J. Güntherodt, A method for the calibration of magnetic force microscopy tips, J. Appl. Phys. **88**, 435 (2000).

[37] J. Schwenk, Multi-modal and quantitative magnetic force microscopy: Application to thin film systems with interfacial Dzyaloshinskii-Moriya interaction, Ph.D. thesis, University of Basel, 2016.

[38] S. Vock, Z. Sasvári, C. Bran, F. Rhein, U. Wolff, N. S. Kiselev, A. N. Bogdanov, L. Schultz, O. Hellwig, and V. Neu, Quantitative magnetic force microscopy study of the diameter evolution of bubble domains in a $(Co/Pd)_{80}$ multilayer, IEEE Trans. Magn. **47**, 2352 (2011).

[39] S. Vock, C. Hengst, M. Wolf, K. Tschulik, M. Uhlemann, Z. Sasvári, D. Makarov, O. G. Schmidt, L. Schultz, and V. Neu, Magnetic vortex observation in FeCo nanowires by quantitative magnetic force microscopy, Appl. Phys. Lett. **105**, 172409 (2014).

[40] M. Baćani, M. A. Marioni, J. Schwenk, and H. J. Hug, How to measure the local Dzyaloshinskii-Moriya Interaction in skyrmion thin-film multilayers, Sci. Rep. **9**, 3114 (2019).

[41] K.-Y. Meng, A. S. Ahmed, M. Baćani, A.-O. Mandru, X. Zhao, N. Bagués, B. D. Esser, J. Flores, D. W. McComb, H. J. Hug, and F. Yang, Observation of nanoscale skyrmions in $SrIrO_3/SrRuO_3$ bilayers, Nano Lett. **19**, 3169 (2019).

[42] A. Yagil, A. Almoalem, A. Soumyanarayanan, A. K. C. Tan, M. Raju, C. Panagopoulos, and O. M. Auslaender, Stray field signatures of Néel textured skyrmions in Ir/Fe/Co/Pt multilayer films, Appl. Phys. Lett. **112**, 192403 (2018).

[43] S. McVitie, R. P. Ferrier, J. Scott, G. S. White, and A. Gallagher, Quantitative field measurements from magnetic force microscope tips and comparison with point and extended charge models, J. Appl. Phys. **89**, 3656 (2001).

[44] A. Fernández Scarioni, C. Barton, H. Corte-León, S. Sievers, X. Hu, F. Ajejas, W. Legrand, N. Reyren, V. Cros, O. Kazakova, and H. W. Schumacher, Thermoelectric Signature of Individual Skyrmions, Phys. Rev. Lett. **126**, 077202 (2021).

[45] See Supplemental Material at http://link.aps.org/supplemental/10.1103/PhysRevB.108.104409 for information on (S1) the magnetic multilayered model used to simulate the skyrmion stray magnetic field; (S2) device fabrication and experimental details; (S3) thermoelectric measurements used to measure global hysteresis loops of the device; (S4) the magnetic and mechanical properties of the MFM probe including the TTF and ICF; (S5) sum of the residuals squared analysis to determine the best-fit case for w; (S6) ambient magnetic force microscopy noise analysis and; (S7) micromagnetic simulations setup. (Also see references therein [46–59]).

[46] W. Legrand, N. Roncenay, D. Maccariello, N. Reyren, V. Cros, and A. Fert, Modeling the Shape of Axisymmetric Skyrmions in Magnetic Multilayers, Phys. Rev. Appl. **10**, 064042 (2018).

[47] R. M. Rowan-Robinson, A. A. Stashkevich, Y. Roussigné, M. Belmeguenai, S.-M. Chérif, A. Thiaville, T. P. A. Hase, A. T. Hindmarch, and D. Atkinson, The interfacial nature of proximity induced magnetism and the Dzyaloshinskii-Moriya interaction at the Pt/Co interface, Sci. Rep. **7**, 16835 (2017).

[48] W. Grange, M. Maret, J.-P. Kappler, J. Vogel, A. Fontaine, F. Petroff, G. Krill, A. Rogalev, J. Goulon, M. Finazzi, and N. B. Brookes, Magnetocrystalline anisotropy in (111) $CoPt_3$ thin films probed by x-ray magnetic circular dichroism, Phys. Rev. B **58**, 6298 (1998).

[49] S. Woo, K. Litzius, B. Krüger, M.-Y. Im, L. Caretta, K. Richter, M. Mann, A. Krone, R. M. Reeve, M. Weigand, P. Agrawal, I. Lemesh, M.-A. Mawass, P. Fischer, M. Kläui, and G. S. D. Beach, Observation of room-temperature magnetic skyrmions and their current-driven dynamics in ultrathin metallic ferromagnets, Nat. Mater. **15**, 501 (2016).

[50] I. Lemesh, F. Büttner, and G. S. D. Beach, Accurate model of the stripe domain phase of perpendicularly magnetized multilayers, Phys. Rev. B **95**, 174423 (2017).

[51] P. Krzysteczko, X. Hu, N. Liebing, S. Sievers, and H. W. Schumacher, Domain wall magneto-Seebeck effect, Phys. Rev. B **92**, 140405(R) (2015).

[52] J. L. Hutter, Comment on tilt of atomic force microscope cantilevers: Effect on spring constant and adhesion measurements, Langmuir **21**, 2630 (2005).

[53] J. L. Hutter and J. Bechhoefer, Calibration of atomic-force microscope tips, Rev. Sci. Instrum. **64**, 1868 (1993).

[54] U. Bostanci, M. Kurtuluş Abak, O. Aktaş, and A. Dâna, Nanoscale charging hysteresis measurement by multifrequency electrostatic force spectroscopy, Appl. Phys. Lett. **92**, 093108 (2008).

[55] D. Nečas and P. Klapetek, GWYDDION: An open-source software for SPM data analysis, Cent. Eur. J. Phys. **10**, 181 (2012).

[56] U. Pietsch, V. Holý, and T. Baumbach, Determination of layer thicknesses of single layers and multilayers, in *High-Resolution X-Ray Scattering*, Advanced Texts in Physics (Springer, New York, 2004).

[57] M. Björck and G. Andersson, GENX: An extensible x-ray reflectivity refinement program utilizing differential evolution, J. Appl. Crystallogr. **40**, 1174 (2007).

[58] B. Sakar, S. Sievers, A. Fernández Scarioni, F. Garcia-Sanchez, Í. Öztoprak, H. Werner Schumacher, and O. Öztürk, A Ti/Pt/Co multilayer stack for transfer function based magnetic force microscopy calibrations, Magnetochemistry **7**, 78 (2021).

[59] W. Legrand, Crafting magnetic Skyrmions at room temperature: Size, stability and dynamics in multilayers, Ph.D. thesis, Universit Paris Saclay, 2019.

[60] I. E. Dzyaloshinskii, Thermodynamic theory of "weak" ferromagnetism in antiferromagnetic substances, Sov. Phys. JETP **5**, 1259 (1957).

[61] T. Moriya, Anisotropic superexchange interaction and weak ferromagnetism, Phys. Rev. **120**, 91 (1960).

[62] C. Moreau-Luchaire, C. Moutafis, N. Reyren, J. Sampaio, C. A. F. Vaz, N. Van Horne, K. Bouzehouane, K. Garcia, C. Deranlot, P. Warnicke, P. Wohlhüter, J.-M. George, M. Weigand, J. Raabe, V. Cros, and A. Fert, Additive interfacial chiral interaction in multilayers for stabilization of small individual skyrmions at room temperature, Nat. Nanotechnol. **11**, 444 (2016).

[63] A. Hrabec, J. Sampaio, M. Belmeguenai, I. Gross, R. Weil, S. M. Chérif, A. Stashkevich, V. Jacques, A. Thiaville, and S. Rohart, Current-induced skyrmion generation and dynamics in symmetric bilayers, Nat. Commun. **8**, 15765 (2017).

[64] M. Heide, G. Bihlmayer, and S. Blügel, Dzyaloshinskii-Moriya interaction accounting for the orientation of magnetic domains in ultrathin films: Fe/W(110), Phys. Rev. B **78**, 140403(R) (2008).

[65] A. Thiaville, R. Stanislas, J. Émilie, V. Cros, and A. Fert, Dynamics of Dzyaloshinskii domain walls in ultrathin magnetic films, EPL **100**, 57002 (2012).

[66] A. Vansteenkiste, J. Leliaert, M. Dvornik, M. Helsen, F. Garcia-Sanchez, and B. Van Waeyenberge, The design and verification of MUMAX3, AIP Adv. **4**, 107133 (2014).

[67] K. Fallon, S. McVitie, W. Legrand, F. Ajejas, D. Maccariello, S. Collin, V. Cros, and N. Reyren, Quantitative imaging of hybrid chiral spin textures in magnetic multilayer systems by Lorentz microscopy, Phys. Rev. B **100**, 214431 (2019).

[68] I. M. Izmozherov, V. V. Zverev, and E. Zh. Baykenov, Bloch lines in thin films with perpendicular magnetic anisotropy and intermediate quality factor, J. Phys.: Conf. Ser. **1389**, 012002 (2019).

[69] A. Bernand-Mantel, L. Camosi, A. Wartelle, N. Rougemaille, M. Darques, and L. Ranno, The skyrmion-bubble transition in a ferromagnetic thin film, SciPost Phys. **4**, 027 (2018).